Highly efficient plasmonic interconnector based on the asymmetric junction between metal-dielectric-metal and dielectric slab waveguides

Seung-Yeol Lee, Junghyun Park, Minsu Kang, and Byoungho Lee*

National Creative Research Center for Active Plasmonics Application Systems, Inter-University Semiconductor Research Center and School of Electrical Engineering, Seoul National University, Gwanak-Gu Gwanakro 599, Seoul 151-744, South Korea
*byoungho@snu.ac.kr

Abstract: A novel interconnection structure that is capable of transferring surface plasmon energy between two distanced metal-dielectric-metal waveguides is proposed. A numerical analysis indicates that the power transferring efficiency of the proposed structure approaches 88.5% for one millimeter of interconnection length. The main mechanism of the proposed interconnector is governed by Fabry-Pérot resonance and a multi-mode interference effect in the junction layers. A physical analysis based on the mechanism for designing an optimized structure is also provided, which could be used to modify the proposed structure.

©2011 Optical Society of America

OCIS codes: (130.2790) Guided waves; (200.4650) Optical interconnects; (250.5300) Photonic integrated circuits; (240.6680) Surface plasmon.

References and links

1. J. A. Dionne, L. A. Sweatlock, M. T. Sheldon, A. P. Alivisatos, and H. A. Atwater, "Silicon-based plasmonics for on-chip photonics," IEEE J. Sel. Top. Quantum Electron. **16**(1), 295–306 (2010).
2. D. A. B. Miller, "Optical interconnects to silicon," IEEE J. Sel. Top. Quantum Electron. **6**(6), 1312–1317 (2000).
3. W. L. Barnes, A. Dereux, and T. W. Ebbesen, "Surface plasmon subwavelength optics," Nature **424**(6950), 824–830 (2003).
4. B. Lee, I.-M. Lee, S. Kim, D.-H. Oh, and L. Hesselink, "Review on subwavelength confinement of light with plasmonics," J. Mod. Opt. **57**(16), 1479–1497 (2010).
5. J. A. Conway, S. Sahni, and T. Szkopek, "Plasmonic interconnects versus conventional interconnects: a comparison of latency, crosstalk and energy costs," Opt. Express **15**(8), 4474–4484 (2007).
6. E. Cubukcu, E. A. Kort, K. B. Crozier, and F. Capasso, "Plasmonic laser antenna," Appl. Phys. Lett. **89**(9), 093120 (2006).
7. S. Kim, H. Kim, Y. Lim, and B. Lee, "Off-axis directional beaming of optical field diffracted by a single subwavelength metal slit with asymmetric dielectric surface gratings," Appl. Phys. Lett. **90**(5), 051113 (2007).
8. S. Kim, Y. Lim, H. Kim, J. Park, and B. Lee, "Optical beam focusing by a single subwavelength metal slit surrounded by chirped dielectric surface gratings," Appl. Phys. Lett. **92**(1), 013103 (2008).
9. B. Lee, S. Kim, H. Kim, and Y. Lim, "The use of plasmonics in light beaming and focusing," Prog. Quantum Electron. **34**(2), 47–87 (2010).
10. S.-Y. Lee, J. Park, I. Woo, N. Park, and B. Lee, "Surface plasmon beam splitting by the photon tunneling through the plasmonic nanogap," Appl. Phys. Lett. **97**(13), 133113 (2010).
11. J. Park, H. Kim, and B. Lee, "High order plasmonic Bragg reflection in the metal-insulator-metal waveguide Bragg grating," Opt. Express **16**(1), 413–425 (2008).
12. Q. Zhang, X.-G. Huang, X.-S. Lin, J. Tao, and X.-P. Jin, "A subwavelength coupler-type MIM optical filter," Opt. Express **17**(9), 7549–7554 (2009).
13. J. Park, H. Kim, I.-M. Lee, S. Kim, J. Jung, and B. Lee, "Resonant tunneling of surface plasmon polariton in the plasmonic nano-cavity," Opt. Express **16**(21), 16903–16915 (2008).
14. B. Lee, S. Roh, and J. Park, "Current status of micro- and nano-structured optical fiber sensors," Opt. Fiber Technol. **15**(3), 209–221 (2009).
15. K. F. Macdonald, Z. L. Sámson, M. I. Stockman, and N. I. Zheludev, "Ultrafast active plasmonics," Nat. Photonics **14**, 55–58 (2008).
16. H. Kim, J. Park, S.-W. Cho, S.-Y. Lee, M. Kang, and B. Lee, "Synthesis and dynamic switching of surface plasmon vortices with plasmonic vortex lens," Nano Lett. **10**(2), 529–536 (2010).
17. W. Cai, J. S. White, and M. L. Brongersma, "Compact, high-speed and power-efficient electrooptic plasmonic modulators," Nano Lett. **9**(12), 4403–4411 (2009).

18. Z. Wu, R. L. Nelson, J. W. Haus, and Q. Zhan, "Plasmonic electro-optic modulator design using a resonant metal grating," Opt. Lett. **33**(6), 551–553 (2008).
19. R. F. Oulton, V. J. Sorger, D. A. Genov, D. F. P. Pile, and X. Zhang, "A hybrid plasmonic waveguide for subwavelength confinement and long-range propagation," Nat. Photonics **2**(8), 496–500 (2008).
20. M. Hochberg, T. Baehr-Jones, C. Walker, and A. Scherer, "Integrated plasmon and dielectric waveguides," Opt. Express **12**(22), 5481–5486 (2004).
21. C. Delacour, S. Blaize, P. Grosse, J. M. Fedeli, A. Bruyant, R. Salas-Montiel, G. Lerondel, and A. Chelnokov, "Efficient directional coupling between silicon and copper plasmonic nanoslot waveguides: toward metal-oxide-silicon nanophotonics," Nano Lett. **10**(8), 2922–2926 (2010).
22. Y. Song, J. Wang, Q. Li, M. Yan, and M. Qiu, "Broadband coupler between silicon waveguide and hybrid plasmonic waveguide," Opt. Express **18**(12), 13173–13179 (2010).
23. J. Tian, S. Yu, W. Yan, and M. Qiu, "Broadband high-efficiency surface-plasmon-polariton coupler with silicon-metal interface," Appl. Phys. Lett. **95**(1), 013504 (2009).
24. Q. Li, Y. Song, G. Zhou, Y. Su, and M. Qiu, "Asymmetric plasmonic-dielectric coupler with short coupling length, high extinction ratio, and low insertion loss," Opt. Lett. **35**(19), 3153–3155 (2010).
25. M. Kang, J. Park, I.-M. Lee, and B. Lee, "Floating dielectric slab optical interconnection between metal-dielectric interface surface plasmon polariton waveguides," Opt. Express **17**(2), 676–687 (2009).
26. G. Veronis and S. Fan, "Theoretical investigation of compact couplers between dielectric slab waveguides and two-dimensional metal-dielectric-metal plasmonic waveguides," Opt. Express **15**(3), 1211–1221 (2007).
27. P. Lalanne and E. Silberstein, "Fourier-modal methods applied to waveguide computational problems," Opt. Lett. **25**(15), 1092–1094 (2000).
28. H. Kim, I.-M. Lee, and B. Lee, "Extended scattering-matrix method for efficient full parallel implementation of rigorous coupled-wave analysis," J. Opt. Soc. Am. A **24**(8), 2313–2327 (2007).
29. E. Prodan, C. Radloff, N. J. Halas, and P. Nordlander, "A hybridization model for the plasmon response of complex nanostructures," Science **302**(5644), 419–422 (2003).
30. H. Kim, J. Hahn, and B. Lee, "Focusing properties of surface plasmon polariton floating dielectric lenses," Opt. Express **16**(5), 3049–3057 (2008).
31. Z. Ahmed, "Schrodinger transmission through one-dimensional complex potential," Phys. Rev. A **64**(4), 042716 (2001).
32. J. A. Dionne, H. J. Lezec, and H. A. Atwater, "Highly confined photon transport in subwavelength metallic slot waveguides," Nano Lett. **6**(9), 1928–1932 (2006).
33. H. J. Lezec, J. A. Dionne, and H. A. Atwater, "Negative refraction at visible frequencies," Science **316**(5823), 430–432 (2007).
34. J. A. Dionne, K. Diest, L. A. Sweatlock, and H. A. Atwater, "PlasMOStor: a metal-oxide-Si field effect plasmonic modulator," Nano Lett. **9**(2), 897–902 (2009).
35. E. D. Palik, *Handbook of Optical Constants of Solids* 2nd ed. (Academic Press, 1998), Chap. 11, 356.

1. Introduction

Crystalline silicon-based technology has led us to the modern digital information era within the last few decades. Recently developed, integrated electronic circuit systems have increased in integration density to keep pace with the rapid increase in the amount of data being handled [1]. However, as the density of integration approaches its limits in terms of fabrication, it is accompanied by an increased circuit delay and higher electronic power dissipation, which is often referred to as "interconnection bottleneck" [1]. Therefore, considerable efforts have been made to develop a new type of data processing method instead of the electrical circuit-based system [1,2]. One of the most promising candidates is the use of surface plasmon polaritons (SPPs), which are collective oscillations between electrons and strong evanescent electric fields on a metal surface [3]. These SPPs have various merits for data processing such as subwavelength confinement characteristics [4], fast signal speed, broad bandwidth, and a low consumption of energy [5]. In addition, for intra-chip interconnections, SPPs have the potential to reduce signal delay and permit low cross-talk [2]. Therefore, wide applications have been intensively researched for using SPPs in the various types of optical devices, such as active sources [6], beaming and focusing of SPP waves [7–9], beam splitters [10], low loss optical filters [11–13], fiber sensors [14], and optical switches [15–18].

However, one of the most significant shortcomings for integrating the above-mentioned SPP-based devices is their overly short propagation length caused by metallic losses [2]. Although considerable efforts have been made to increase the intrinsic propagation length of SPP modes [19], more than the millimeter scale of transport length is needed for much larger scale interconnections such as chip-to-chip and layer-to-layer interconnections. Therefore, for those types of large scale interconnection, a technology is needed that will permit the efficient coupling from SPP modes to photonic waveguides. Since the coupling structure between the

SPP mode and conventional silicon waveguides was demonstrated [20], many researchers have studied these SPPs-to-photonic mode couplers with various structures [21–24].

In our previous work, we proposed an interconnection structure for connecting two distanced SPP modes on metal-dielectric (MD) waveguides [25]. However, these SPP modes in MD waveguides have a relatively poor confinement characteristic which is distributed up to a few micrometers. Furthermore, since the longer evanescent tail of the SPP mode of an MD waveguide causes more scattering losses at the interface between the MD waveguide and the dielectric slab waveguide, our previous work cannot provide a high performance for near-infrared frequencies, which is the most commonly used wavelength in optical communication systems. The metal-dielectric-metal (MDM) waveguide, which has a core of a thin dielectric layer and metal cladding, has good confinement characteristics and the propagation length of the MDM waveguide is also comparable to that of the MD waveguide. Since it has many useful points for connecting distanced MDM waveguide modes rather than MD waveguide modes, many efforts have been made to couple the MDM modes to a photonic mode, such as a direct junction or complicated junction width design through an optimizing algorithm [26]. But these efforts mainly suffer from a high amount of reflection loss.

In this paper, we propose a novel interconnection structure for distanced MDM plasmonic waveguides. Instead of the previously reported direct and symmetric junctions [26], we propose an asymmetric and indirect junction which has a thin MD layer for the mid-gap layer. It turns out that the dielectric slab, floated between the ends of MD layers, can efficiently transfer the plasmonic mode to the photonic mode through a stepwise mode transition. The high scattering loss shown in our previous work can also be suppressed by adapting the MDM plasmonic waveguide. The efficiency of the overall structure approaches 88.5% of the total power transition for 1 mm of transition length and the loss that occurs as the result of an interconnection junction is less dependent on the overall length of the dielectric slab waveguide. We also provide design rules for optimizing an interconnector structure with appropriate physical features, to make it helpful for understanding these kinds of interconnector. The design method could also be applied to further modification of the structure.

2. Overall structure view and optimized result

Figure 1(a) shows the overall structure of the proposed MDM interconnector. The structure can be viewed as two parts: input and output connectors. A sufficiently long dielectric slab waveguide is floated between each side of the connector. The structure can transform the surface plasmon mode into the guided photonic mode in the dielectric slab, and can efficiently transport surface plasmon energy without any metallic losses in that region. The operation wavelength of the interconnector is set to 1550 nm. As shown in Fig. 1(a), design parameters for the proposed structure include the thickness of the MDM plasmonic waveguide (t_{core}), the thickness of the gap between the dielectric slab and metal layer (t_{gap}), the thickness of the dielectric slab waveguide (t_{slab}), the length of the dielectric slab waveguide (L_{slab}), the length of the overlapped region ($L_{overlap}$), and the length of the gap region between the slab waveguide and the MDM plasmonic waveguide (L_{MD}).

By adopting the appropriate optimization process based on the results presented in the following sections, the MDM-to-MDM interconnector can be optimized as depicted in Fig. 1(b). The color bar denotes the y-directional magnetic field. The overall efficiency (P_o/P_I) for this structure, obtained by integrating the Poynting vector, was determined to be 90.5% for $L_{slab} = 6$ μm.
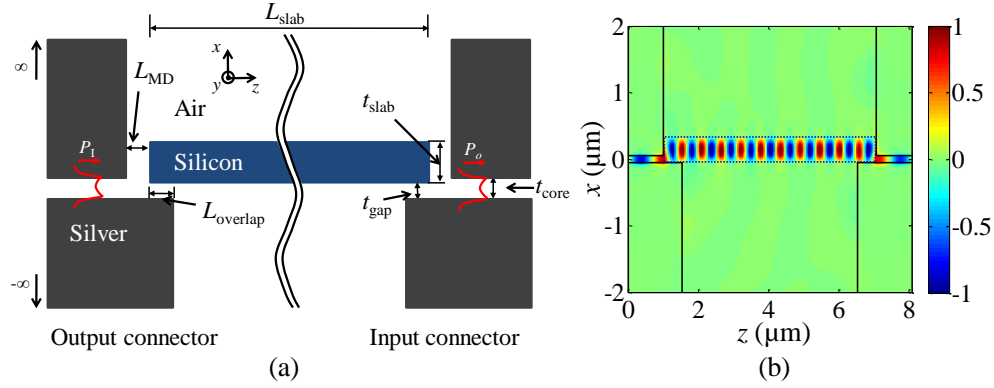
Fig. 1. (a) The overall structure of the MDM interconnector including both input and output connectors. (b) The y-directional magnetic field distribution of the optimized interconnector structure (Media 1). Design parameters are set to t_{core} = 100 nm, t_{gap} = 10 nm, t_{slab} = 370 nm, L_{slab} = 6 µm, $L_{overlap}$ = 500 nm, and L_{MD} = 40 nm. The permittivity of silicon and silver is given as ε_{Si} = 11.7 and ε_{Ag} = −86.6 + 8.7i, respectively [35].

Although we show the case of a relatively short dielectric slab, the efficiency still remains still high even in the case for the L_{slab} on a millimeter scale. This can be ascribed to the fact that the origin of loss in dielectric slab region is only related to the material loss of the silicon slab waveguide.

Most of our simulation results were obtained by using the rigorous coupled wave analysis (RCWA) method. This algorithm is advantageous since it is convenient for extracting the coupling power of specific eigenmodes [27,28] from the numerical calculation. In order to support only the single MDM mode and to provide sufficient guiding confinement, the value of t_{core} is fixed at 100 nm throughout our overall simulations, except for the simulation shown in Fig. 6(c) in Section 4. Other parameters will be optimized to obtain the best performance of the proposed interconnector with an appropriate physical analysis. The detailed calculation method for the single-side connector and the junction mechanism is dealt with in the following sections.

3. Analysis of the single-sided connecter

3.1 Field coupling mechanism for output connector

As mentioned in the previous section, the MDM plasmonic interconnector structure can be split into two parts: the output connector and the input connector. We will analyze the output side of the connector first. Figure 2(a) depicts the structure of the output connector of the MDM interconnector with a field coupling diagram. There are several factors that can cause losses of output connector. First, when the incident MDM SPP mode (the amount of power is P_I) reaches the end of the MDM waveguide layer, some portion of the power is directly reflected (P_R) at the interface. Next, some other losses associated with the mode difference between MDM and MD layers and the multiple reflections inside the MD layer exist. Some of these losses that leak through the upper-side passageway, which are referred to as primary leakage loss (P_{Leak1}), can be a surface mode as well as a scattering far field mode, as shown in Fig. 2(a). In the overlapped layer, the SPP mode propagating along the MD layer transfers its power to the dielectric slab waveguide mode via coupling to the hybrid modes generated in overlapped region. Therefore, the power coupled to the dielectric slab waveguide is very sensitive to the length of the overlapped layer. When the power is not efficiently transferred from the overlapped layer to the dielectric slab layer, the secondary leakage loss (P_{Leak2}), leaking waves from the end of the overlapped layer and multiple reflections inside the overlapped layer are simultaneously increased.
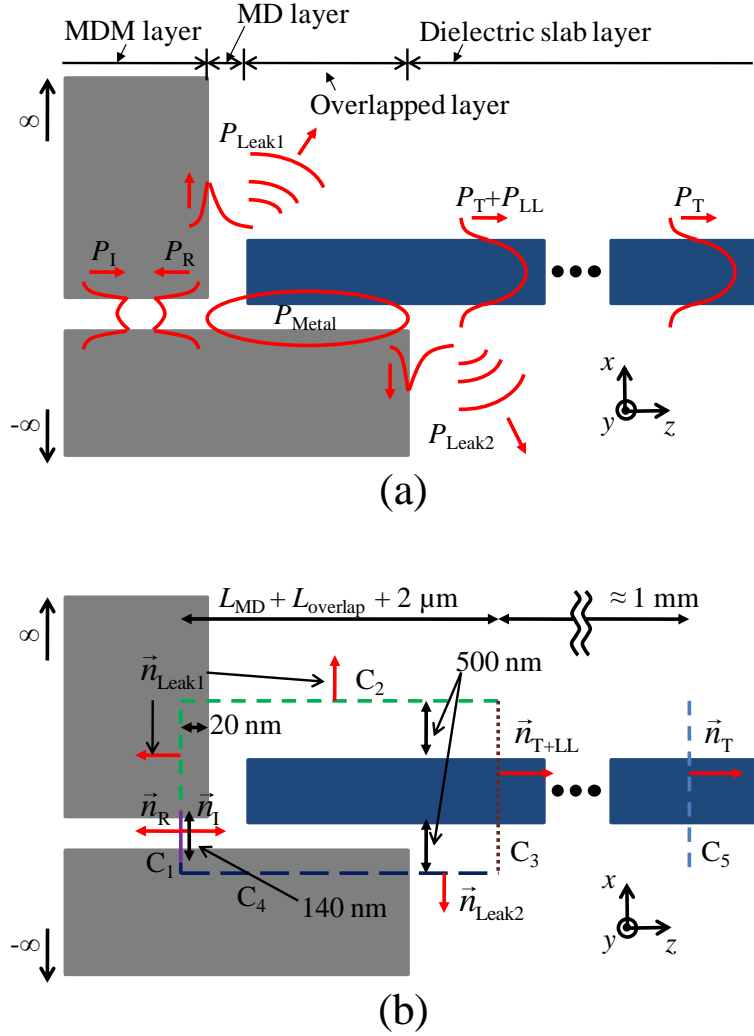
Fig. 2. (a) A schematic for defining the name of each layer and each type of field coupled at the output connector structure. (b) A schematic for defining the contours and normal vectors which are used for calculation of each type of power.

Moreover, the multiple reflections inside the MD and overlapped layer finally decay by thermal loss of the metal layer (P_{Metal}) or they can change the amount of direct reflection loss. Finally, long-range leakage loss (P_{LL}) will occur, which will eventually disappear and only the propagating modes will remain (P_{T}).

Each type of power is calculated by the contour integration of the Poynting vectors. Figure 2(b) shows the contours of the integration and their normal vectors. The amount of the power can be obtained as

$$P_{type} = \int_{C_i} (\vec{E} \times \vec{H}^*) \times \vec{n}_{type} \, dl \quad (i = 1, 2, 3, 4, 5; \; type = R, T, LL, Leak1, Leak2). \quad (1)$$

Due to the nature of the RCWA simulation, it is possible to turn the specific mode on or off. To separate P_I and P_R, we turn off the incident field when we measure P_R, and turn off the reflected field when we measure P_I. The energy conservation law requires

$$P_I = P_R + P_T + P_{LL} + P_{Leak2} + P_{Leak2} + P_{Metal}. \quad (2)$$

Table 1 summarizes various types of the losses of output connector and their detailed calculation methods.

Table 1. Types of the Coupling Power and their Calculation Methods

Type	Description	Calculation Methods
P_I	Incident power	$\int_{C_1} (\vec{E} \times \vec{H}^*) \times \vec{n}_I \, dl$, reflected field off
P_R	Reflected power at the end of MDM layer	.. incident field off
P_T	Coupling power to the propagating modes of the dielectric slab	$\int_{C_5} (\vec{E} \times \vec{H}^*) \cdot \vec{n}_T \, dl$
P_{LL}	Coupling power which will eventually disappear for long-range propagation	$\int_{C_3} (\vec{E} \times \vec{H}^*) \cdot \vec{n}_{T+LL} \, dl - \int_{C_5} (\vec{E} \times \vec{H}^*) \cdot \vec{n}_T \, dl$
P_{Leak1}	Leaked power through the upper side of MD layer	$\int_{C_2} (\vec{E} \times \vec{H}^*) \cdot \vec{n}_{Leak1} \, dl$
P_{Leak2}	Leaked power at the end of the overlapped layer	$\int_{C_4} (\vec{E} \times \vec{H}^*) \cdot \vec{n}_{Leak2} \, dl$
P_{Metal}	Metallic loss	$P_I - (P_R + P_T + P_{LL} + P_{Leak1} + P_{Leak2})$

3.2 Synthetic analysis for the optimization of the output connector

In this section, we analyze each type of coupled power described in Section 3.1 by changing the design parameters shown in Section 2. Figures 3(a)–3(f) show each type of coupled power ratio for various values of $L_{overlap}$ and t_{gap}. In Fig. 3(a), periodic modulation of P_T is shown with variation in the $L_{overlap}$ when the t_{gap} value is lower than 50 nm. When the high refractive index slab is floated on the metal surface, two different types of hybrid modes can exist [25,29]. The insets of Fig. 3(f) show the mode profile of both modes, the first being a plasmonic hybrid mode, which is mostly guided through the gap between metal and dielectric slab, whereas the second hybrid mode is a photonic hybrid mode, which is guided in the dielectric slab rather than metallic interface. In the overlapped layer, the coupling coefficients of both modes are changed periodically due to the multimode interference effect of both modes. Therefore, the period of the transferring power is determined by the phase matching condition:

$$\Lambda_1 = \frac{\lambda_0}{\left| n_{plasmonic} - n_{photonic} \right|}. \tag{3}$$

Here, λ_0 is the free space wavelength; $n_{plasmonic}$ and $n_{photonic}$ are the effective refractive indexes of plasmonic and photonic hybrid modes in overlapped layer, respectively. For the case of t_{gap} = 10 nm, $n_{plasmonic}$ and $n_{photonic}$ are determined to be 1.73 and 2.99, respectively. The period of transferring power is thus calculated to be Λ_1 = 1.23 μm. However, this relation can be satisfied only when two hybrid modes are tightly coupled. If t_{gap} value gets thicker, these modal interferences are reduced and the amount of P_T is also decreased. In this case, the coupling mechanism is mainly governed by the Fabry-Pérot effect of the plasmonic hybrid mode in the overlapped layer. This is clearly shown in Fig. 3(b), in which the P_R is changed periodically and the period is quite different from the value obtained using Eq. (3). The value of $n_{plasmonic}$ is obtained as 1.17 and the period of resonance shown in Fig. 3(b) is approximately 660 nm for the case of t_{gap} = 180 nm, which is almost the same as the resonance condition for Fabry-Pérot resonator:

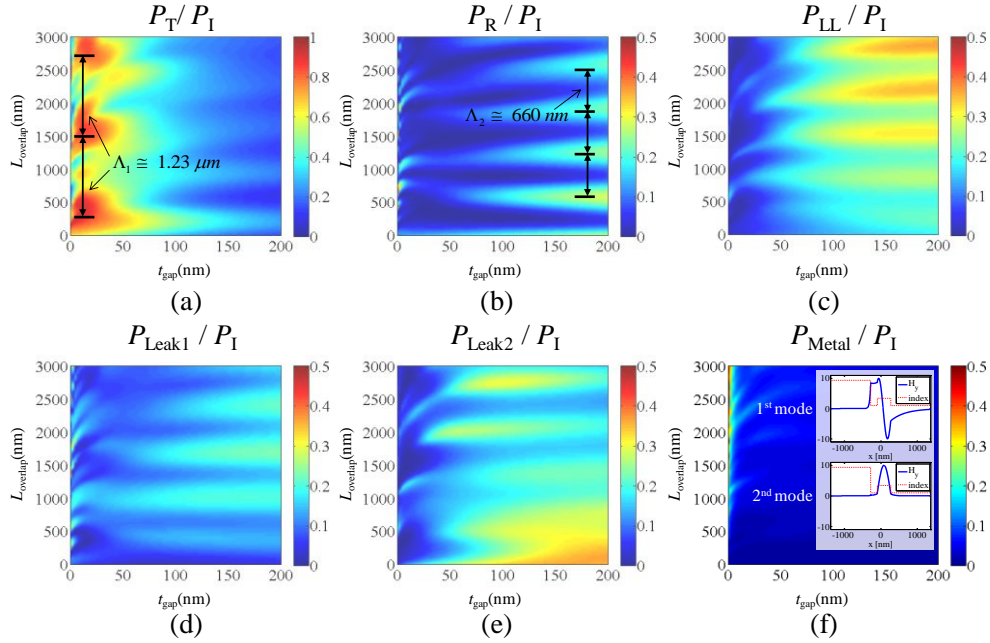$$\Lambda_2 = \frac{\lambda_0}{2 n_{plasmonic}}. \tag{4}$$

Fig. 3. (a)-(f) The amount of the calculated power depicted in Table 1 when the values of t_{gap} and $L_{overlap}$ are varied. Each type of power is normalized by the incident power P_I. Two types of hybrid modes are shown in the insets of (f).

Although these resonances may affect the reflected power, it is not clearly shown in transmitted power. This is due to the fact that these Fabry-Pérot resonances occur by the plasmonic hybrid mode in the overlapped layer. At the end of the layer, most of the energy of the plasmonic hybrid mode is scattered into the far field since the mode shape of the plasmonic hybrid mode is quite different from that of the dielectric slab mode. This leakage power is clearly shown in Figs. 3(c) and 3(e).

In addition, the value of P_T rapidly decreases when the dielectric slab is contacted or is floating very slightly. There are two reasons for why this phenomenon occurs. One is the severe effective index difference between the MDM layer and the overlapped layer, which generates large amounts of reflected power. This can be seen in the left end side of Fig. 3(b). The other reason is the rapid decrease in the propagation length in the overlapped layer. The SPP mode in the overlapped layer has much more losses when the dielectric slab is in contact rather than floating [30]. Since this loss is caused by the lossy metal, it increases proportionally with $L_{overlap}$ as shown in Fig. 3(f). Therefore, we should avoid the contacted dielectric slab in order to obtain high P_T value.
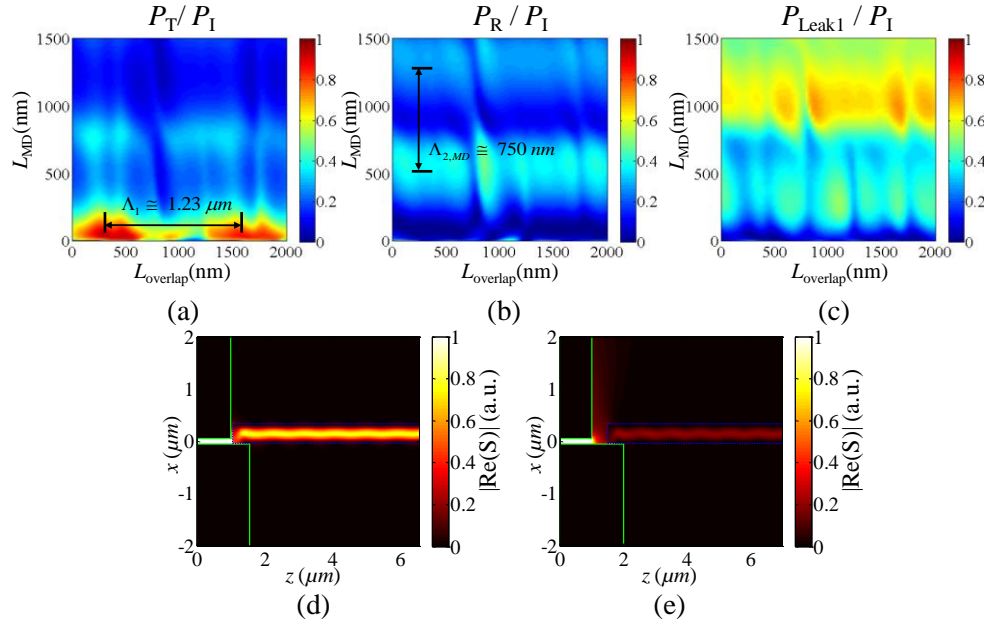
Fig. 4. (a)-(c) The amount of transmitted, reflected, and primary leaked power normalized by the incident power P_I when the design parameters L_{MD} and $L_{overlap}$ are varied. Magnitude of the power flow distribution of the output connector with (d) L_{MD} = 50 nm and (e) L_{MD} = 500 nm, respectively. All the other parameters are the same as in Fig. 1(b) except for the infinite L_{slab}.

In Figs. 4(a)–4(c), we present the ratio of P_T, P_R, and P_{Leak1} normalized by P_I as functions of $L_{overlap}$ and L_{MD}. Since the value of t_{gap} is fixed to 10 nm, the coupling mechanism in the overlapped layer is governed by a modal interference effect, which results in the periodic modulation with the period calculated by Eq. (3) and this is clearly demonstrated in Fig. 4(a). Instead, the Fabry-Pérot effect in the overlapped layer is relatively weak, so that there is no strong modulation with the $L_{overlap}$ value in P_R and P_{Leak1}. When the value of L_{MD} is changed, Fig. 4(b) shows periodic modulation with a period of 750 nm, which is the same as what the Fabry-Pérot resonance period accounts for by the SPP mode in MD layer. The slight enhancement in P_T value at L_{MD} = 800 nm is due to a reduction in P_R. However, the P_T value gradually decreases with increasing value of L_{MD}. A high P_T with low P_{Leak1} can be obtained only when the L_{MD} is in the subwavelength scale. Unlike our previous work [25], the scattering waves cannot propagate in a backward direction, since they are blocked, and most are coupled to the evanescent field components of the surface mode propagating along the vertical interface between the MDM and MD layers. However, these powers are almost re-coupled to the dielectric slab waveguide when L_{MD} is sufficiently short. This is extensively compared in Figs. 4(d) and 4(e), which illustrates the magnitude of the Poynting vector ($\vec{S}$) when the value of L_{MD} is 50 nm and 500 nm, respectively.

In summary, the points below might be helpful for achieving a high power transmission.

- The $L_{overlap}$ value might be chosen with the consideration of the periodic modulation caused by modal interference between two hybrid modes in the overlapped layer.

- A longer $L_{overlap}$ value results in more metallic losses.

- The contacted dielectric slab (t_{gap} = 0) has a significant reflection and metallic loss compared to the results for a slightly floated slab and an overly thick t_{gap} value cannot efficiently couple the SPP mode due to weak modal interferences.

- A longer L_{MD} value results in more primary leakage loss due to the low coupling efficiency of the evanescent field generated at the end of the MDM layer; however, an overly short L_{MD} causes high reflection losses.

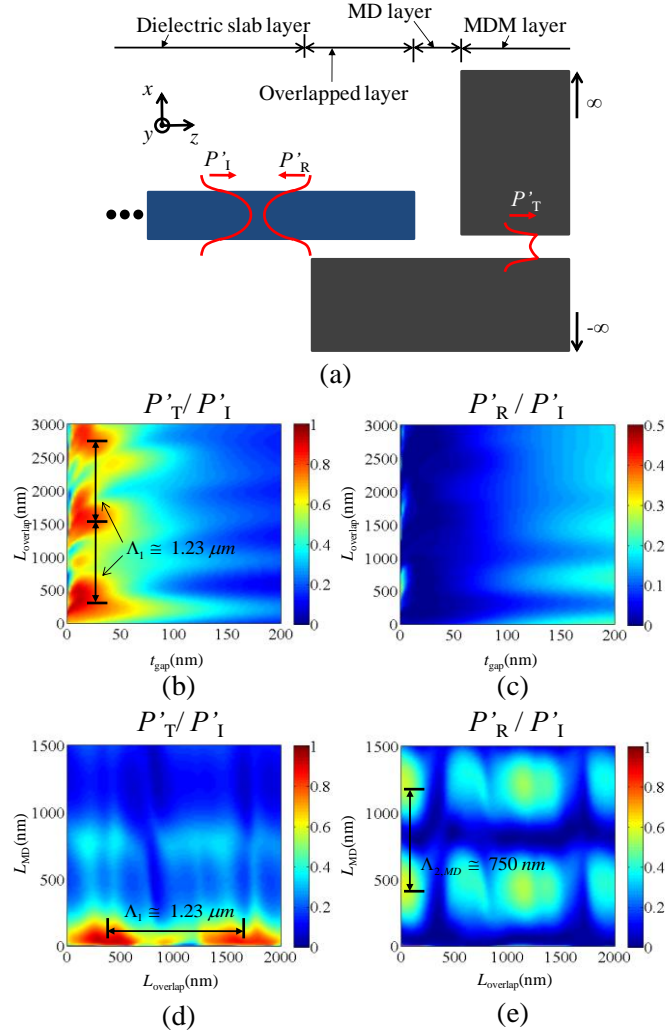*3.3 Analysis for the optimization of the input connector*

(a)

(b)

(c)

(d)

(e)

Fig. 5. (a) Schematic diagram of the input connector structure. (b), (c) Amount of transmitted and reflected power of the input connector normalized by the incident power P'_I when the design parameters t_{gap} and $L_{overlap}$ are varied. (d), (e) same transmitted and reflected power ratio for the case when the parameters L_{MD} and $L_{overlap}$ are varied.

A schematic diagram of input connector is shown in Fig. 5(a). In this case, we analyze only the reflection and transmission power since the coupling mechanism and resonance condition are almost the same as that in the output connector. The incident mode is assumed to be the fundamental photonic mode of dielectric slab waveguide. This assumption is only satisfied when the t_{slab} is below the single mode cutoff thickness or in the case where the power is almost coupled to the fundamental mode although t_{slab} is above the single mode cutoff thickness. This condition is well-satisfied when t_{slab} is below 400 nm, which will be shown in next section.

The same parameter sweeping results are shown in Figs. 5(b)–5(e). The transmission characteristics of the input connector are quite similar to that of the output connector, whereas the reflection characteristics are different from those of the output connector due to the non-symmetric feature of each connector [31]. One of the significant differences is that the Fabry-Pérot-like resonance effect by the $L_{overlap}$ value is much weaker than that of the output connector for a thicker t_{gap} as shown in Fig. 5(c). This is reasonable since the difference between the effective refractive indexes of the modes of the dielectric slab layer and overlapped layer is much smaller than that for the overlapped and MD layers. Next, by comparing Figs. 4(b) and 5(e), the vertical lines are more vividly shown, which indicates that the modal interference effect in the overlapped layer more sensitively affects the reflection power.

4. Analysis of the overall interconnector structure

So far, we have discussed on a useful method for obtaining a high transmission ratio for a one-sided connector. However, since the transmission characteristics of the interconnector should be almost independent of the variation of the L_{slab} value, it is not sufficient to design an efficient interconnector structure without an analysis of its total structure.
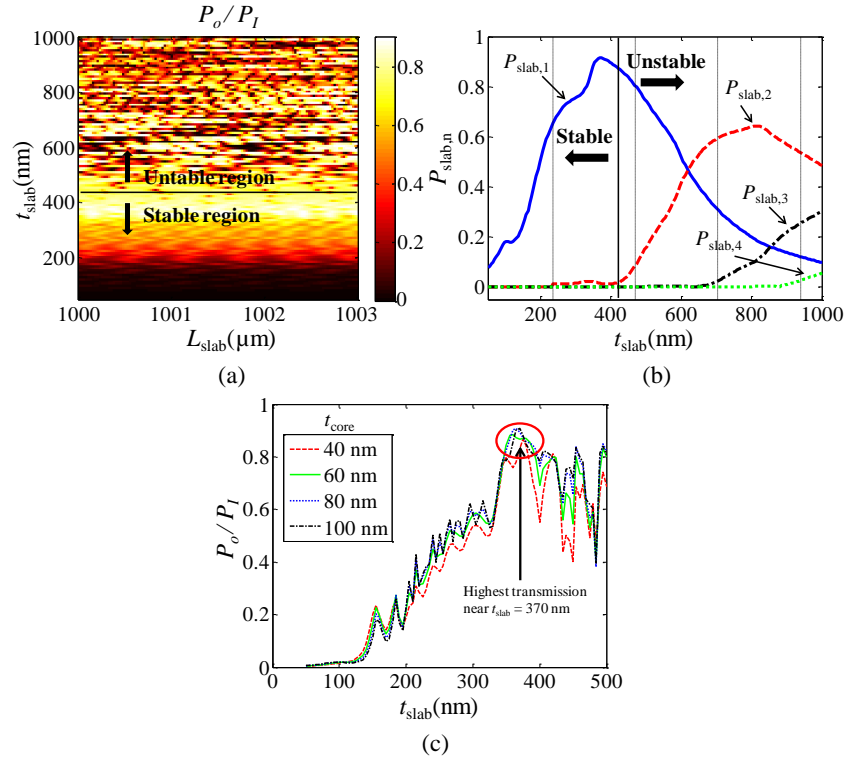

Fig. 6. (a) The overall transmission power ratio (P_o / P_I) is shown with the variation in parameters L_{slab} and t_{gap}. All the other parameters are the same as Fig. 1(b). (b) The mode coupling ratios for each order of mode in the dielectric slab layer are shown. Vertical black dashed lines denote the cutoff thickness of each dielectric slab mode. (c) Relationships between the overall transmission power ratio and the MDM core thickness are shown.

In Fig. 6(a), the overall transmission power is shown when L_{slab} and t_{gap} are changed. We categorized the transmission characteristics in this figure into three regions; the first one is, as mentioned in Ref [25], the region in which the value of t_{slab} is lower than the single mode cutoff thickness. In this region, the transmission characteristic is almost uniform with respect to variation in L_{slab}, however the coupling ratio is too low due to leakage losses which are

explained in a previous section. The second region, which shows a different result from our previous results [25], is not included in the single mode region but shows both uniform and high transmission characteristics. In this region, even though two propagating modes are supported, the coupling ratio to the secondary mode is very small as shown in Fig. 6(b). Both regions are included on the stable region of Fig. 6(a). When the t_{slab} value is higher than these two regions, severe degradation in the stability of transmission characteristics occurs. The criteria of these regions are mainly dependent on the mode coupling ratio ($P_{slab,n}$) rather than the cutoff thickness; the mode coupling ratio is defined by

$$P_{slab,n} = \frac{\text{Coupled power to } n^{th} \text{ order dielectric slab mode}}{\text{Incident power}}. \tag{5}$$

The peak of the fundamental mode coupling ratio ($P_{slab,1}$) appears near the 370 nm of the t_{slab} value, and this point is well-matched with the highest P_o/P_i line in Fig. 6(a), and it also gives stable transmission characteristics with the variation in the value of L_{slab}. Above the 400 nm of the value of t_{slab}, $P_{slab,1}$ gradually decreases, whereas coupling to the higher-order propagating modes is increased and the multimode interference effect in dielectric slab layer leads to unstable transmission characteristics.

Finally, we checked the dependency of our structure as a function of the thickness of the t_{core} value, which is depicted in Fig. 6(c). When the core width of the MDM waveguide becomes narrower, the overall efficiency is reduced slightly. This may originate from an increase in the effective refractive index of the MDM plasmonic waveguide mode, which can make more direct reflection loss at the interface of the MDM and MD layers. Nevertheless, it appears that the overall efficiency is not sensitive to the value of t_{core}, compared with the other parameters such as t_{slab}. The highest transmission efficiency is usually in the same region (near $t_{slab} = 370$ nm), regardless of the t_{core}. Therefore, we expect that our structure is not quite sensitive to the t_{core} value, which can be variously applied to the different thickness of the MDM plasmonic waveguides.

5. Modification of the proposed structure for use in practical devices

Although our interconnector structure provides efficient transmission characteristics with a simple geometry, some additional issues still remain for this structure to be used as a practical device. Firstly, the structure has a narrow air gap inside the MDM layer and the overlapped layer. The gap might be implemented by inserting small balls into the gap. However, since the fabrication of the structure is not easily realized, we propose the modified structure shown in Fig. 7(a).
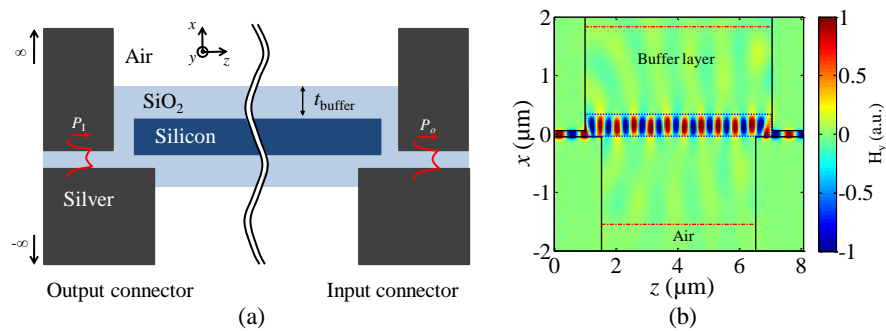

Fig. 7. (a) Schematic diagram of the overall interconnector structure with an additional buffer layer. (b) The y-directional magnetic field distribution of the interconnector structure with buffer layer. All design parameters are the same as the case of Fig. 1(b), except for the additional parameter $t_{buffer} = 1.5$ μm.

The air gap inside the MDM layer and overlapped layer can be filled with SiO$_2$, which has a relatively lower refractive index ($n = 1.5$) than silicon. Moreover, if we encapsulate the

silicon slab waveguide with the buffer layer of SiO_2, we can get two advantageous factors: preventing the silicon slab layer from bending, and improving the mode coupling efficiency by reducing the effective mode index difference with the SiO_2-filled MDM plasmonic waveguide. Figure 7(b) shows the y-directional magnetic field distribution, which has a similar field profile to that shown in the Fig. 1(b). Although the overall efficiency (P_o/P_I) is slightly decreased to 84.6%, this value is still sufficiently high. Note that no additional optimization process was considered for the SiO_2-filled case.

Another critical issue for our interconnector structure is the y-directional confinement characteristic, since the waveguide for an integrated optical circuit should be confined to the lateral direction. Several experimental results have been reported, showing that the characteristics of a three-dimensional (3D) MDM slot waveguide with a sufficiently wide lateral confinement follow approximately those of the two-dimensional (2D) MDM slab waveguide [32–34]. In order to demonstrate this similarity between the 2D and 3D cases, we carried out a 3D finite difference time domain (FDTD) simulation for the interconnection structure between two distanced MDM slot waveguides.
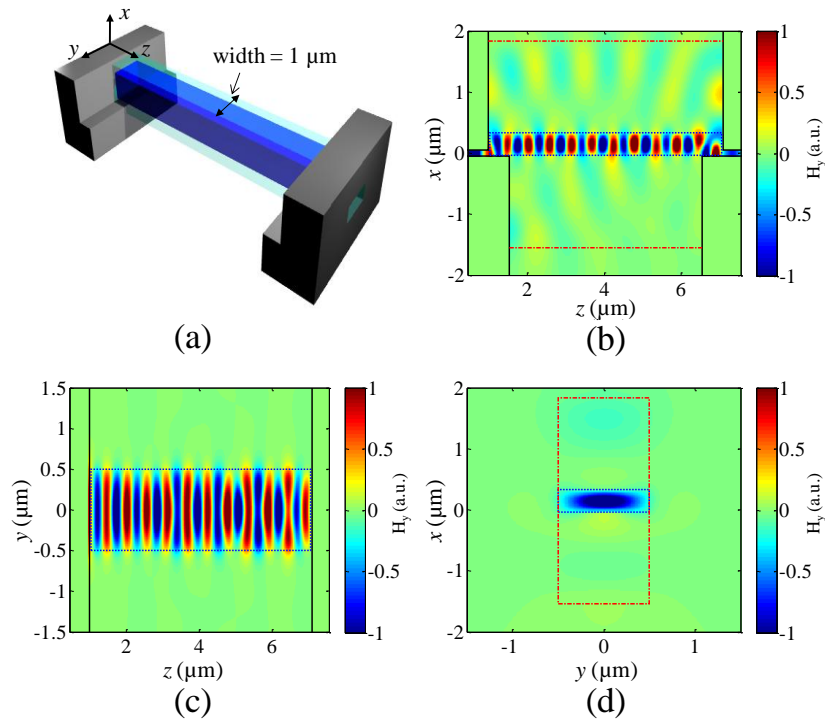
Fig. 8. (a) 3D schematic of the proposed interconnector structure. The widths of the MDM slot waveguide and dielectric slot waveguide are set to 1 μm. (b)-(d) The y-directional magnetic field distribution on the cutoff plane of (b) $y = 0$, (c) $x = 100$ nm, and (d) $z = 0$, respectively. All the other design parameters are same as the case of Fig. 7(b).

Figure 8(a) shows the 3D structure of the overall structure with SiO_2 buffer layer. The magnetic field distributions for the x-z, y-z, and x-y cutoff planes of this structure are depicted in Figs. 8(b), 8(c), and 8(d), respectively. The findings indicate that the field distribution for the x-z cutoff plane is almost same as Fig. 7(b); the only difference is a slight decrease in field uniformity inside the silicon slab. We assume that the reason for this decreased uniformity originate from the y-directional confinement, which is shown in Fig. 8(c). However it does not dramatically affect the overall efficiency of the structure. Most of the field is confined to the high index silicon slot waveguide; therefore it can be concluded that our structure still exhibits good confinement characteristics for a 3D configuration. For this simulation, the overall

transmission efficiency was determined to be 77.6%. Although this value is somewhat lower than the optimized efficiency of 88.5%, we expect that the transmission efficiency for 3D interconnector structure could reach a value higher than 77.6%, since we did not consider any additional optimization process for the 3D structure.

6. Conclusion

We proposed an efficient interconnector structure that can transport the SPP mode from one MDM waveguide to another MDM waveguide via a floated dielectric slab waveguide located on the metal surface. By utilizing the MDM waveguide rather than the MD waveguide, scattering losses could be suppressed and a higher transmission is achieved. The asymmetric junction of the input and output connectors could enhance the transmission efficiency by an efficient plasmonic-to-photonic mode conversion mechanism between photonic and plasmonic modes existing in the overlapped layer. The transmission characteristic of overall interconnector, including both sides of the connector, does not substantially change below the specific cutoff condition which is directly determined by the mode coupling energy inside the dielectric region. Moreover, our structure still has a high performance even with the various modifications such as a variation in core thickness or a 3D configuration. Therefore, we expect that our results could provide a useful strategy for transferring the surface plasmon energy for long distances with very small metallic losses, and it could be applied to chip-to-chip interconnections of plasmonic integrated circuit systems.

Acknowledgment